Earth and Planetary Science Letters 430 (2015) 235–248

Contents lists available at ScienceDirect

Earth and Planetary Science Letters

www.elsevier.com/locate/epsl

Geochemistry and thermodynamics of an earthquake: A case study of pseudotachylites within mylonitic granitoid

Hehe Jiang [a,*], Cin-Ty A. Lee [a], Julia K. Morgan [a], Catherine H. Ross [a,b]

[a] Department of Earth Science, Rice University, Houston, Texas, United States
[b] Department of Earth and Planetary Sciences, McGill University, Montreal, Quebec, Canada

ARTICLE INFO

Article history:
Received 13 May 2015
Received in revised form 8 August 2015
Accepted 19 August 2015
Available online xxxx
Editor: A. Yin

Keywords:
mylonitic granitoid
pseudotachylite
brittle deformation
biotite
frictional melting
Peninsular Ranges

ABSTRACT

Pseudotachylites are melts produced by frictional heating during seismic slip. Understanding their origin and their influence on slip behavior is critical to understanding the physics of earthquakes. To provide insight into this topic, we conducted a case study in the proto-mylonitic to mylonitic Asbestos Mountain granitoid in the eastern Peninsular Ranges batholith (California), which records both ductile (mylonites) and brittle deformation features (pseudotachylites and ultracataclasites). U–Pb chronology and Zr thermometry of titanite porphyroblasts in the mylonites indicate that mylonitization of the plutons occurred at near solidus conditions (~750 °C) over a 10 Ma interval from 89 to 78 Ma. Mylonitization resulted in recrystallization of quartz, plagioclase and biotite, with the biotite concentrated into biotite-rich foliation planes. Subsequent brittle deformation is superimposed on the ductile fabrics. Micro-XRF elemental mapping and in situ LA-ICP-MS analyses on these brittle deformation products show that the pseudotachylites are more mafic (lower Si, but higher Fe) and K-rich than the host mylonite, while the ultracataclasites are intermediate between the host and the pseudotachylites. Inverse mass balance calculations show that both brittle deformation products are depleted in quartz but enriched in biotite, with the pseudotachylites showing the most significant enrichment in biotite, indicating preferential involvement of biotite during brittle deformation. We suggest that biotite-rich layers generated during ductile deformation may have been the preferred locus of subsequent brittle deformation, presumably because such layers represent zones of weakness. Frictional heating associated with slip along such planes results in melting, which causes a decrease in viscosity, in turn leading to further strain localization. During the short time span of an earthquake, frictional melting appears to be a disequilibrium process, in which the minerals are melted in order of their melting points, from biotite (~800 °C) to plagioclase (~1400 °C) and finally to quartz (~1700 °C), rather than by equilibrium melting, which results in silicic eutectoid melts at lower temperatures (~650 °C). Thus, with progressive slip, melt composition should evolve from mafic to felsic, eventually approaching the bulk composition of the host rock. The mafic composition of the pseudotachylites thus indicates that they formed between the melting point of biotite and plagioclase (800–1400 °C). Our chemical and modeling analyses on the pseudotachylites suggest that the chemical composition of pseudotachylites can potentially be used to constrain the thermodynamic conditions in the shear zone as well as earthquake source mechanics.

© 2015 Elsevier B.V. All rights reserved.

1. Introduction

Pseudotachylites are quenched melt produced along a fault surface by friction-induced heating associated with seismic slip. Thus, pseudotachylites may provide information on physical properties of the fault and the thermodynamics of the slip process (Sibson, 1975; Maddock, 1983; Magloughlin and Spray, 1992; Spray, 1995; Wenk et al., 2000; Di Toro et al., 2009; Spray, 2010). Pseudotachylites commonly occur in shear zones, where they are often spatially associated with ductile fabrics, forming networks of veins and dikes within and cross-cutting the foliation of the host rock (Wenk et al., 2000; Di Toro et al., 2009; Pittarello et al., 2012). This coexistence of pseudotachylites and foliated host rocks suggests that there may be a casual relation between ductile deformation and brittle deformation: because seismic slip commonly occurs along pre-existing planes of weakness, such as phyllosilicate-defined fabrics (Collettini et al., 2009; Niemeijer et al., 2010), the question arises as to whether the locus of brittle deformation is inherited or influenced by pre-existing ductile fabrics. To

* Corresponding author.
E-mail address: hehe.jiang@rice.edu (H. Jiang).

http://dx.doi.org/10.1016/j.epsl.2015.08.027
0012-821X/© 2015 Elsevier B.V. All rights reserved.

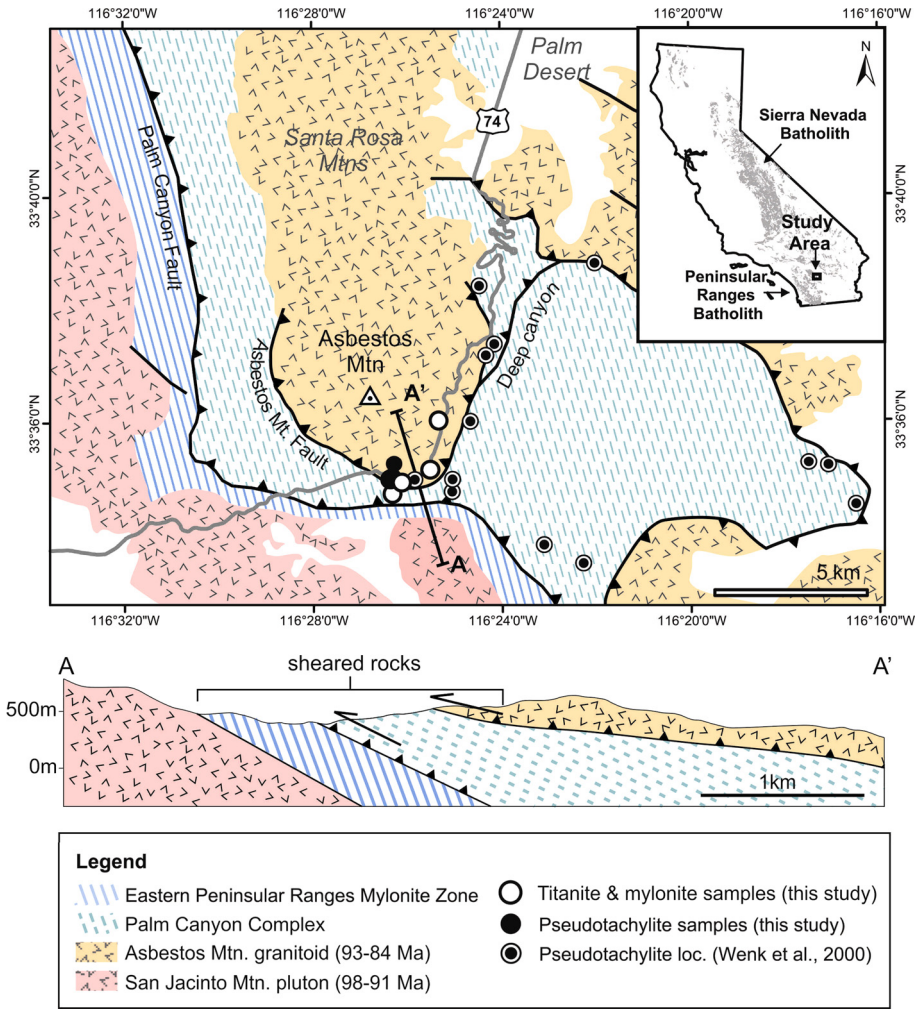

Fig. 1. Regional geologic map of the Santa Rosa Mountains, modified from Simpson (1984), Todd et al. (1988) and Wenk et al. (2000). Zircon U–Pb ages of the San Jacinto Mountain and Asbestos Mountain plutons are from Premo et al. (2014).

answer this question, it is crucial to understand how the ductile fabrics are developed and how different mineral phases in the deformed host rock, especially those that constitute the fabrics, contribute to brittle deformation. Here we explore how the geochemistry of deformation products provides insight into localization and thermodynamics of brittle deformation. We present a combined textural, geochronologic and geochemical study of ductile and brittle deformation products in a Late Cretaceous shear zone in the northeastern Peninsular Ranges batholith in southern California (USA). In this shear zone, ductile deformation developed under middle to upper crustal conditions during cooling of a large granitoid batholith. As a consequence, the shear zone records an entire deformational sequence from weakly deformed granitoid plutonic rocks to strongly foliated mylonites with biotite-defined fabrics. Superimposed on this ductile fabric is evidence of extensive brittle deformation in the form of pseudotachylites and ultracataclasites (Simpson, 1984; Todd et al., 1988; Wenk et al., 2000; Rowe et al., 2012). We investigated the duration and temperature of mylonitic fabric development, and tracked the geochemical signature of major minerals (plagioclase, quartz and biotite) in both ductile and brittle deformation products. We report direct geochemical evidence that biotite-rich foliation planes are the primary locus for brittle deformation, confirming the inheritance of brittle deformation from ductile fabric. To explain the composition of the pseudotachylites, we preformed simple thermal modeling to simulate thermal and stress evolution in the shear zone. We show that the presence of biotite constrains the thermodynamics of brittle deformation. We also propose that the extent to which the composition of the pseudotachylites deviates from that of their host rock is strongly linked to earthquake source properties, such as the magnitude and duration of an earthquake.

2. Geologic background

The Peninsular Ranges batholith (PRB) is part of the mid- to late Cretaceous Cordillera arc formed on the western margin of the North American continental crust during eastward subduction of the Farallon oceanic plate. The northeastern PRB in southern California was emplaced during successive magmatic episodes between 100 and 80 Ma (Morton et al., 2014; Premo et al., 2014). Top-to-southwest thrusting occurred within the batholith during the Late Cretaceous, resulting in an east-dipping shear zone extending from Palm Springs to the southern Santa Rosa Mountains. Evidence of ductile deformation, such as development of mylonitic fabrics, extends from the eastern Peninsular Ranges mylonite zone into the structurally lowest part of the Asbestos Mountain granitoid (Fig. 1) (Simpson, 1984; Erskine and Wenk, 1985; Todd et al., 1988; Morton et al., 2014).

The uppermost part of this shear zone, the Asbestos Mountain granitoid constitutes the hanging wall of the Asbestos Mountain fault, which is one of the low-angle, east-dipping faults kinematically associated with ductile deformation in the shear zone

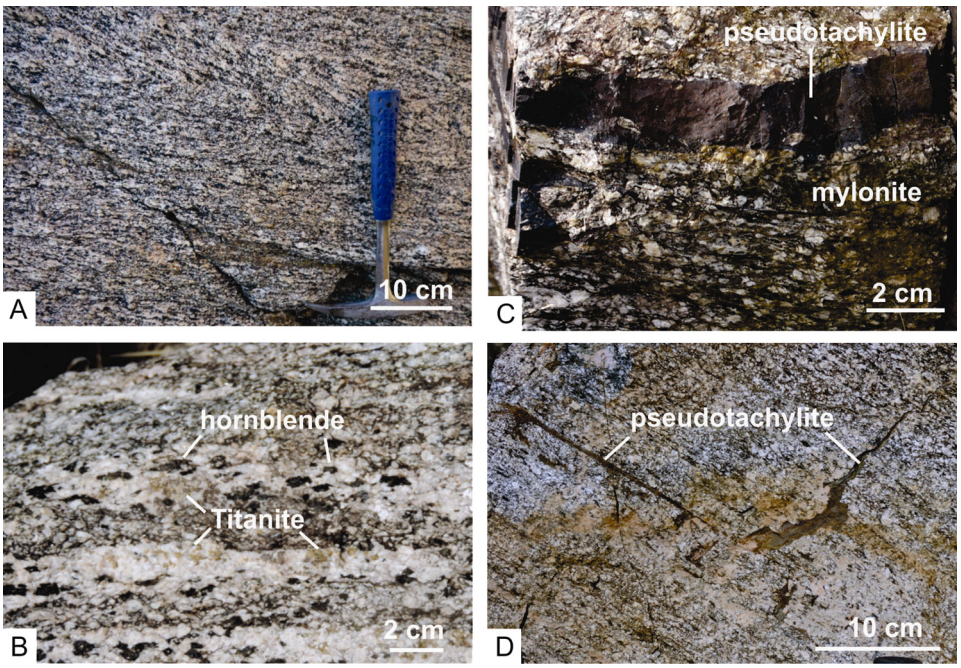

Fig. 2. Field photos of the mylonite and pseudotachylite. (A) Mylonitic fabrics in the tonalite. (B) Felsic lenses with large titanite crystals in the mylonitized granitoid. (C) Pseudotachylite vein subparallel to the mylonitic fabric. (D) Thin pseudotachylite vein parallel to the mylonitic fabric and injection vein cutting into the mylonite.

(Todd et al., 1988). Above the Asbestos fault, sheets of the lower Asbestos Mountain granitoid are characterized by strong east-dipping proto-mylonitic to mylonitic foliations defined by aligned aggregates of biotite and hornblende (Fig. 2A). This contrasts with the weakly-deformed granitoids to the north and east (Fig. 3A). Todd et al. (1988) suggested that the presence of the foliations in the granitoids is indicative of emplacement of plutons during deformation. The bottom part of the foliated granitoid is locally juxtaposed with mylonitic metasedimentary rocks, anatexites and orthogneisses from the Palm Canyon metamorphic complex that comprises the footwall of the Asbestos Mountain fault.

Dark veins or selvages of ultracataclasite and pseudotachylite of variable thicknesses (2 mm–10 cm) are distributed in the vicinity of the Palm Canyon Fault and are locally abundant in the lower Asbestos Mountain granitoid (Wenk et al., 2000; Rowe et al., 2012). The ultracataclasites and pseudotachylites are either parallel to, or cross-cutting the mylonitic foliation, indicating that brittle deformation postdated the ductile mylonitization (Fig. 2C, D). Locally, injection veins are developed from the main pseudotachylite and ultracataclasite veins (Fig. 2D). Studies by Rowe et al. (2012) suggest that they were formed by overpressures (10^2–10^4 kbar) that exceed the rock elastic limit, confirming a paleo-seismic origin for both pseudotachylites and injections. Wenk et al. (2000) found that the occurrence of the ultracataclasites and pseudotachylites is restricted to biotite-rich rocks, suggestive of a potential genetic link between biotite and the brittle deformation products, though they did not themselves attribute any causal relationship. $^{40}Ar/^{39}Ar$ ages of the pseudotachylites suggests that brittle deformation mostly took place between 62 and 56 Ma (Wenk et al., 2000), although all of these ages exhibited very poor plateau characteristics so the uncertainties on such ages could be quite large. The presence of these brittle deformation features suggests that ambient temperature was below 300 °C during the episode of brittle deformation. The transition from ductile to brittle regime is possibly due to rapid post-magmatism exhumation in the eastern Peninsular Ranges area during the Late Cretaceous (Goodwin and Renne, 1991; Wenk et al., 2000).

3. Petrography

Samples of undeformed granitoid, mylonitic granitoid, titanite grains, pseudotachylite and ultracataclasite were collected from the Asbestos Mountain granitoid along and below Highway 74 (Fig. 1 and Supplementary Table S1 for sample locations). Mineralogical and geochemical analyses were conducted to determine the conditions for proto-mylonitic and mylonitic texture development and the contribution of different minerals to brittle deformation.

3.1. Ductile deformation products: tonalitic mylonites

The undeformed granitoids are coarse-grained hornblende-biotite tonalites and retain primary plutonic textures as evidenced by the randomly oriented grains of quartz, plagioclase, biotite and hornblende, ranging from subhedral to euhedral in shape (Fig. 3A). In the mylonites (Fig. 3B), quartz has recrystallized as evidenced by significant grain size reduction. Plagioclase only shows slight reduction in grain size and, in many cases, these minerals may be better considered as porphyroclasts. Most biotites are finely recrystallized and strongly re-oriented to form mylonitic fabrics. Locally, biotite is intergrown with hornblende. Some biotite grains are bent around large plagioclase porphyroclasts.

Conditions for development of the biotite-rich fabrics can be determined from syn-tectonic metamorphic minerals. Of particular interest is the presence of abundant euhedral titanite ($CaTiSiO_5$) with various sizes (<1 mm to >4 cm in longest dimension) aligned with the fabrics in the granitoid. Small grains (<2 mm) are pervasive throughout the entire Asbestos Mountain granitoid, and likely have an igneous origin. However, large titanite crystals with numerous quartz and feldspar inclusions are only found in the mylonitic or proto-mylonitic parts of the granitoid, and they are mostly concentrated in felsic-rich lenses which are also along the foliation (Figs. 2B, 3C). These large crystals were clearly formed through overgrowth of titanite in fluid-rich melts during the last stages of the plutons magmatic life or during mylonitization. Therefore, geochronologic and thermometric constraints from

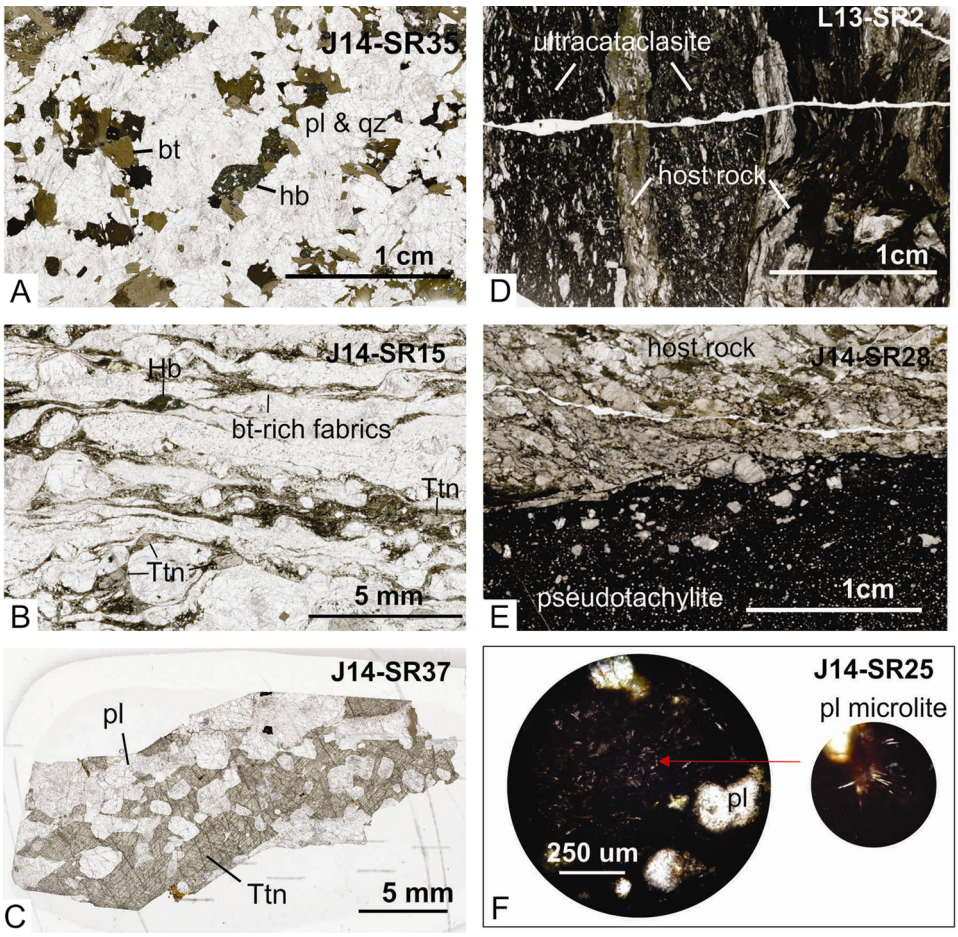

Fig. 3. Thin-section microphotograph of tonalite, mylonite, ultracataclasite and pseudotachylite from the Asbestos Mountain granitoid. (A) Undeformed tonalite sample J14-SR35, showing typical phaneritic texture of plutonic rock. (B) Mylonite sample J14-SR15, showing biotite (bt)-rich fabrics, and accommodation of deformation around large plagioclase (pl) crystals, and distribution of titanites (Ttn). (C) Typical large titanite with quartz and plagioclase inclusions from the mylonite. (D) Ultracataclasite veins in the mylonite, with fine grained matrix and angular quartz and feldspar clasts. (E) Pseudotachylite veins in the mylonitized granitoid. (F) Plane-polarized light photograph of pseudotachylite, showing glass matrix, rounded plagioclase clasts and abundant plagioclase microlites.

the large titanite grains may help bound the timing of mylonitization and the temperatures involved.

3.2. Brittle deformation products: ultracataclasites and pseudotachylites

Both ultracataclasites and pseudotachylites are sub-parallel or cross-cutting the mylonite foliation, showing abrupt contact with the host rock (Fig. 3D, E). The ultracataclasites are characterized by ~10–20% angular rock and mineral fragments supported by a fine-grained (<20 μm) matrix, which we interpret to indicate an origin by mechanical comminution (Fig. 3D). Most clasts are elongated and aligned, indicative of localized shear deformation.

The pseudotachylites, by contrast, are characterized by ~10% rounded clasts in a dark glassy matrix with abundant plagioclase microlites, suggesting quenching of a melt and possible reaction of the melt with entrained clasts. Most clasts are crystal fragments of quartz and plagioclase, often serving as nucleation sites for the microlite growth. There is no alignment and deformation of the microlites, indicating reduction of shear deformation during quenching of the melt.

Locally, ultracataclasite veins are found along the margin of the pseudotachylites (Fig. 6B). Wenk et al. (2000) observed fragments of cataclasites in the pseudotachylite veins, suggesting a genetic relation between the ultracataclasite and pseudotachylite.

4. Geochronologic and geochemical methods

4.1. In situ U–Pb dating for titanite

Twenty-six titanite crystals in six samples were analyzed for U–Pb isotopes by Laser Ablation Inductively Coupled Plasma Mass Spectrometry (LA-ICP-MS) using a ThermoFinnigan Element 2 magnetic sector mass spectrometer equipped with a New Wave 213 nm laser ablation system at Rice University. The instrument was tuned to achieve sensitivity of 700,000–1,000,000 cps for ^{238}U in zircon standard 91500 (Wiedenbeck et al., 1995) with a 30 μm spot size, 10 Hz repetition rate and 9–11 J/cm^2 laser fluence. Analyses for the zircon standard and titanite samples were conducted under the same instrument conditions. ^{204}Pb, ^{206}Pb, ^{207}Pb and ^{208}Pb were measured under counting mode, while ^{232}Th and ^{238}U were measured under analog mode. For all isotopes, we set the mass window at 5% and 60 samples per peak, which gives 3 slices per peak. Settling time for each isotope at each slice is 0.001 s. Sample time for each slice is 0.01 s for ^{204}Pb, ^{206}Pb, ^{208}Pb, ^{232}Th and ^{238}U, and 0.02 s for ^{207}Pb, summing to 0.28 s for one scan cycle. A total of 500 scan cycles were acquired in each measurement. Total data acquisition for each sample is ~114 s, including 15–20 s background acquisition prior to firing the laser, followed by ~100 s of sample acquisition during ablation. Analyses of unknowns were bracketed by analyses of zircon 91500 (TIMS ^{206}Pb/^{238}U age: 1062.4 ± 0.4 Ma) (Wiedenbeck et al., 1995). Ter-

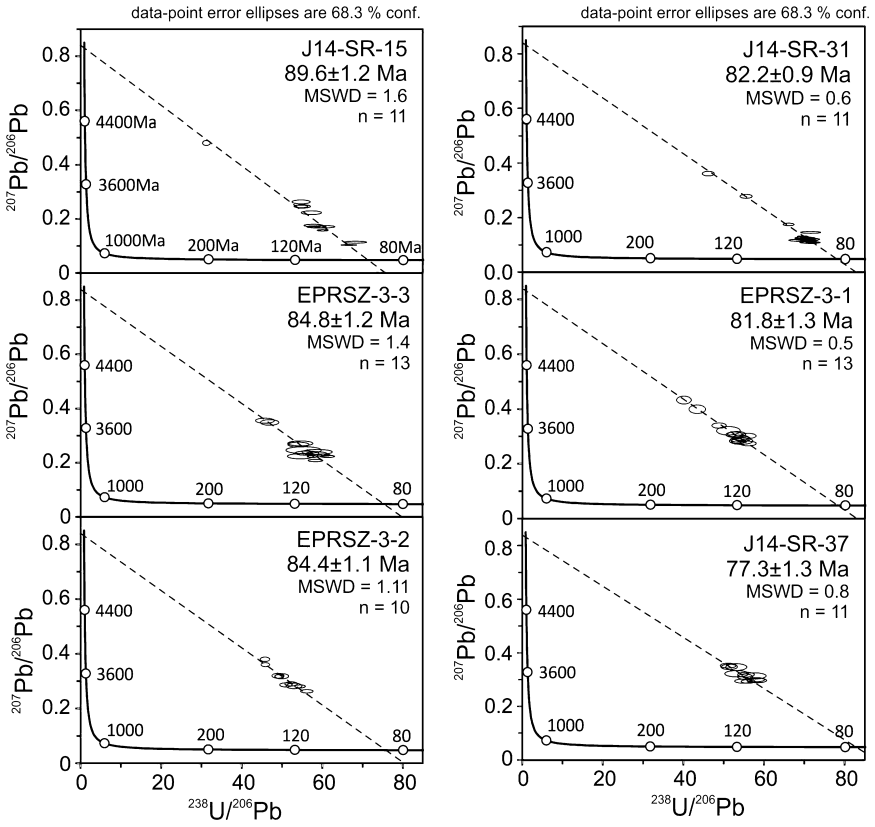

Fig. 4. Tera–Wasserburg diagrams for in-situ analyses of titanite U–Pb isotopes. Each ellipse represents one measurement and 1σ standard deviation. EPRSZ-3-1, EPRSZ-3-2, EPRSZ-3-3, J14-SR-37 are single large titanite crystals (diameter > 0.5 cm). J14-SR-15 and J14-SR-31 are rock samples, and each measurement is from different titanite grains. Uncertainties for the error ellipses are at 68.3% confidence interval (1σ). Age uncertainties are quoted as 95% confidence interval (2σ).

tiary titanite from Fish Canyon Tuff, California (FCT) (TIMS age: 28.395 ± 0.078 Ma) (Schmitz and Bowring, 2001) and Proterozoic metamorphic titanite from Bear Lake Road, Ontario, Canada (BLR) (TIMS age: 1047.1± 0.4 Ma) (Aleinikoff et al., 2007) were also included in each run as monitors of accuracy. Data reduction was done with an in-house Excel-Visual Basic program. Average background intensities are first subtracted from sample intensities. Time-dependent downhole fractionation was corrected by applying a least squares linear regression through all background-corrected Pb/U and Pb/Th ratios back to the initiation of ablation signal. After background subtraction and downhole fractionation correction, isotopic ratios were corrected for instrumental mass bias by normalizing to zircon 91500, which was similarly corrected for down-hole fractionation. The above instrumental setting and data reduction scheme gives a long-term (January to June, 2014) precision of ±0.4% and ±0.6% (2σ, $n = 115$) for background- and fractionation-corrected $^{238}U/^{206}Pb$ and $^{207}Pb/^{206}Pb$ of the zircon standard 91500.

Both the titanite standards and unknowns are heterogeneous in $^{238}U/^{206}Pb$ and $^{207}Pb/^{206}Pb$ isotopic ratios due to variable incorporation of common Pb. When each analysis from the same sample is plotted on a Tera–Wasserburg diagram, this heterogeneity often results in a $^{238}U/^{206}Pb$ and $^{207}Pb/^{206}Pb$ isochron (strictly speaking, this chord is a mixing array between radiogenic and common Pb). The age of the titanite can be calculated as the lower intercept $^{238}U/^{206}Pb$ age on the concordia. Construction of Tera–Wasserburg diagrams and age determination were done using ISOPLOT (Ludwig, 2012). Using a common Pb composition from the Pb evolution model of Stacey and Kramers (1975), titanite standards FCT and BLR yield ages of 28.5 ± 0.3 Ma (2σ, $n = 91$) and 1040 ± 8 Ma (2σ, $n = 80$), consistent with their TIMS ages. For unknowns, we forced the regression through a common $^{207}Pb/^{206}Pb$ ratio of 0.842 ± 0.01, appropriate for crustal differentiation ages between 0 and 250 Ma, again using the Stacey–Kramers model. Tera–Wasserburg diagrams for the unknowns are in Fig. 4. Pb/U, Pb/Th and Pb/Pb ratios are in Supplementary Table S2. Uncertainties for individual analyses are reported at the 68.3% confidence interval (1σ) (Supplementary Table S2, Fig. 4). Typical measurement uncertainty of an isochron age for the unknowns is ~1.6% (2σ). When combined with uncertainties in the isotopic ratios of the zircon standard 91500 and the U decay constants (Jaffey et al., 1971), the total uncertainty for the age of an unknown is ~1.8% (2σ).

4.2. In situ major and trace element analyses

Titanite and hornblendes in the host mylonites, pseudotachylite and ultracataclasite were analyzed in polished thick sections or epoxy mounts by the same LA-ICP-MS system described above. The instrument was tuned to achieve sensitivity of 250,000–350,000 cps for 15 ppm La in basalt standard BHVO2g with 55 μm or 80 μm spot sizes, 10 Hz repetition rate and 12–16 J/cm^2 laser fluence. BHVO2g, BCR2g and BIR1g (Gao et al., 2002) were used as external standards and were analyzed at the beginning and end of each analytical session. Samples were measured under the same instrumental condition with the standards. Major elements were measured in medium mass resolution mode ($m/\Delta m = 3000$), while trace elements were measured in low mass resolution mode ($m/\Delta m = 300$).

We applied 55 μm spot size for measurements of the titanite porphyroblasts and hornblendes, and 80 μm spot size for measurements of ultracataclasite and pseudotachylite matrices. The 80 μm spot size is larger than the microlites in the pseudotachylites and the fine grains making up the matrix in the ultracataclasites, but small enough that most clasts in the pseudotachylites can be

avoided. This allows us to determine a bulk average composition of the pseudotachylite melts and the comminuted matrix of the ultracataclasites.

An in-house Excel-Visual Basic data reduction program (http://www.cintylee.org/#/facilities/) was used to correct for background, drift, instrumental bias and convert raw data to concentrations. ^{44}Ca was used as internal standard to correct for instrumental drift. Data for titanite, hornblende, pseudotachylites and ultracataclasites are in Supplementary Tables S3–S5.

4.3. Elemental mapping by micro-XRF

Elemental mapping of thick blocks of the ultracataclasites and pseudotachylites was carried out using a Horiba XGT-7200 X-ray analytical microscope at Rice University. This instrument is equipped with an X-ray guide tube of either 50 µm or 400 µm diameter with an Rh target. It emits a high-energy micro X-ray beam up to 50 kV and 1 mA. Elements from Na to U can be detected by an energy-dispersive Si drift detector. Elemental mapping was done for major elements under full vacuum condition, with an acceleration voltage of 50 kV, 50 µm capillary, 200–400 s survey time per-frame, and 5 accumulations.

5. Development of biotite-rich mylonitic texture

The U–Pb ages of the titanite range from 89–78 Ma (Fig. 4), which are slightly younger than the zircon U–Pb ages of the Asbestos Mountain granitoid (93–84 Ma from Premo et al., 2014). Sizes of the 26 dated titanite range from 0.5 mm to over 1 cm, but there is no size-dependent trend in the age. Given that the closure temperature of U–Pb system is greater than 900 °C in zircon, and 650–800 °C in titanite (Lee et al., 1997; Spencer et al., 2013), the titanite ages indicate that mylonitization initiated no later than 89 Ma, and thus shortly after the emplacement of plutons in the upper plate zone. This is consistent with the synchronous plutonic emplacement and mylonitization hypothesis proposed by Todd et al. (1988) and also indicates that the ductile textures were developed during cooling of the pluton.

We estimated temperature of mylonitization from titanite formation temperatures using the Zr-in-titanite calibration of Hayden et al. (2008), which assumes zircon saturation and depends on pressure and activity of TiO_2 in the system. Zircon saturation in the PRB tonalites is confirmed by whole-rock Zr systematics (Lee and Bachmann, 2014). Zr concentrations in the same titanite porphyroblasts for which we obtained age data show inter-grain variations from 310 to 600 ppm, but only minor zonation within the grains (Fig. 5). The diffusive length scale of Zr in titanite is only a few microns over a 10 Ma period at temperatures of 600–800 °C, much smaller than the mm to cm size of our titanite grains (Cherniak, 2010b). Therefore, the Zr temperatures reflect the conditions of titanite growth rather than post-growth diffusive re-equilibration. The lack of zonation in the large grains indicates that individual grains nucleated and grew at relatively constant temperature. To estimate the pressure, we measured major elements in hornblendes in the granitoids and calculated the Al-in-hornblende pressures using the calibration of Schmidt (1992). The hornblendes give pressures of ~5.7 kbar (~20 km depth), consistent with previous estimates (5–6.5 kbar) by Ague and Brimhall (1988) using an earlier calibration of the barometer (Hammarstrom and Zen, 1986). The presence of titanites in the rock suggests a high TiO_2 activity ($a_{TiO_2} > 0.5$) (Hayden et al., 2008), therefore we calculated the Zr-in-titanite temperature assuming a range of a_{TiO_2} between 0.5 and 1 (detailed Zr-in-titanite temperature results for $a_{TiO_2} = 0.5$, 0.8 and 0.1 are in Supplementary Table S3). We obtain temperature bounds between 720 and 800 °C, which are well below the liquidus temperature of a dry tonalite but above the water-saturated temperature of tonalite (Huang and Wyllie, 1975).

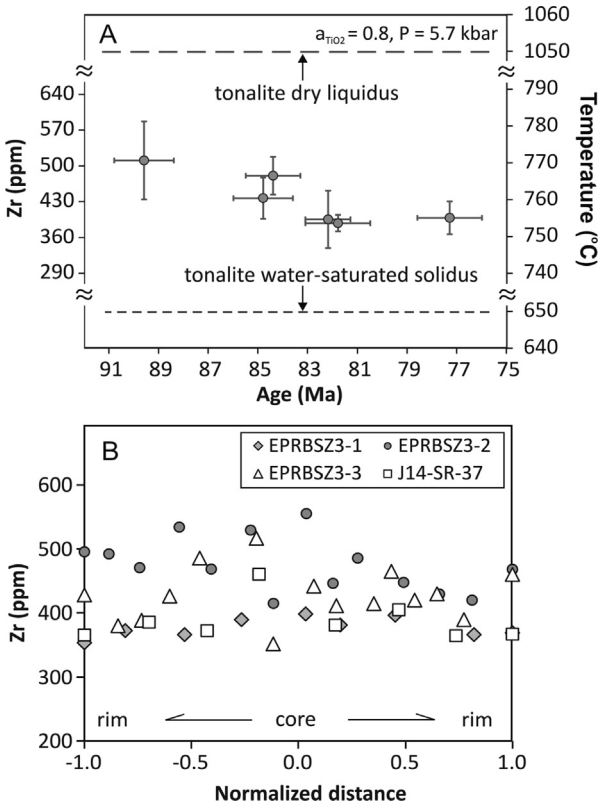

Fig. 5. (A) Zr concentrations and temperature evolution of the titanite from the mylonite. Each data point represents average of ages (Fig. 4) and Zr concentrations (or temperatures) from the same sample. Vertical error bars are the standard deeviations for multiple LA-ICP-MS measurements in the same sample. Zr-in-titanite temperature is calculated from Hayden et al. (2008), using a pressure of 5.7 kbar and Ti activity of 0.8. Dashed line represents the wet solidus and dry liquidus of tonalite at pressure of 6 kbar (Huang and Wyllie, 1975). (B) Zr transects for four large titanite crystals, showing only minor zonation in Zr concentration. The "normalized distance" is calculated as x/r, where x is the position of measurement, and r is the half-length of the total measured distance (~1–2 mm smaller than the radius of the titanite) (r = 1.8, 1.8, 2.9 and 4 mm for EPRSZ3-1, EPRSZ3-2, EPRSZ3-3 and J14-SR37, respectively).

In Fig. 5, we plot Zr-in-titanite temperatures calculated at $a_{TiO_2} = 0.8$ versus U–Pb ages. It can be seen that temperature remains almost constant with at most a 30 °C decrease during the 10 My interval of mylonitization. These relatively uniform, near solidus temperatures in the titanites spanning a 10 My age interval suggest that mylonitization took place shortly after the emplacement of the upper plate zone plutons during the final stages of crystallization. Farner et al. (2014) and Lee et al. (2015) showed that most of the latent heat is released under the final stages of crystallization of wet magmas, resulting in thermal arrest at near-solidus conditions during pluton cooling. Therefore, our Zr temperatures and U–Pb ages in the titanites suggest that ductile deformation occurred when the pluton was a crystalline mush with small amounts of interstitial residual melt. Within this slow cooling pluton, regional deformation caused the biotites to recrystallize and re-orient, resulting in the development of strong biotite-defined foliations, which ultimately, transformed the plutonic rock into anisotropic mylonites.

6. Geochemical evidence for preferential involvement of biotite-rich fabrics in brittle deformation

Relative contributions of different mineral phases from the host rock in brittle deformation can be determined from the geochem-

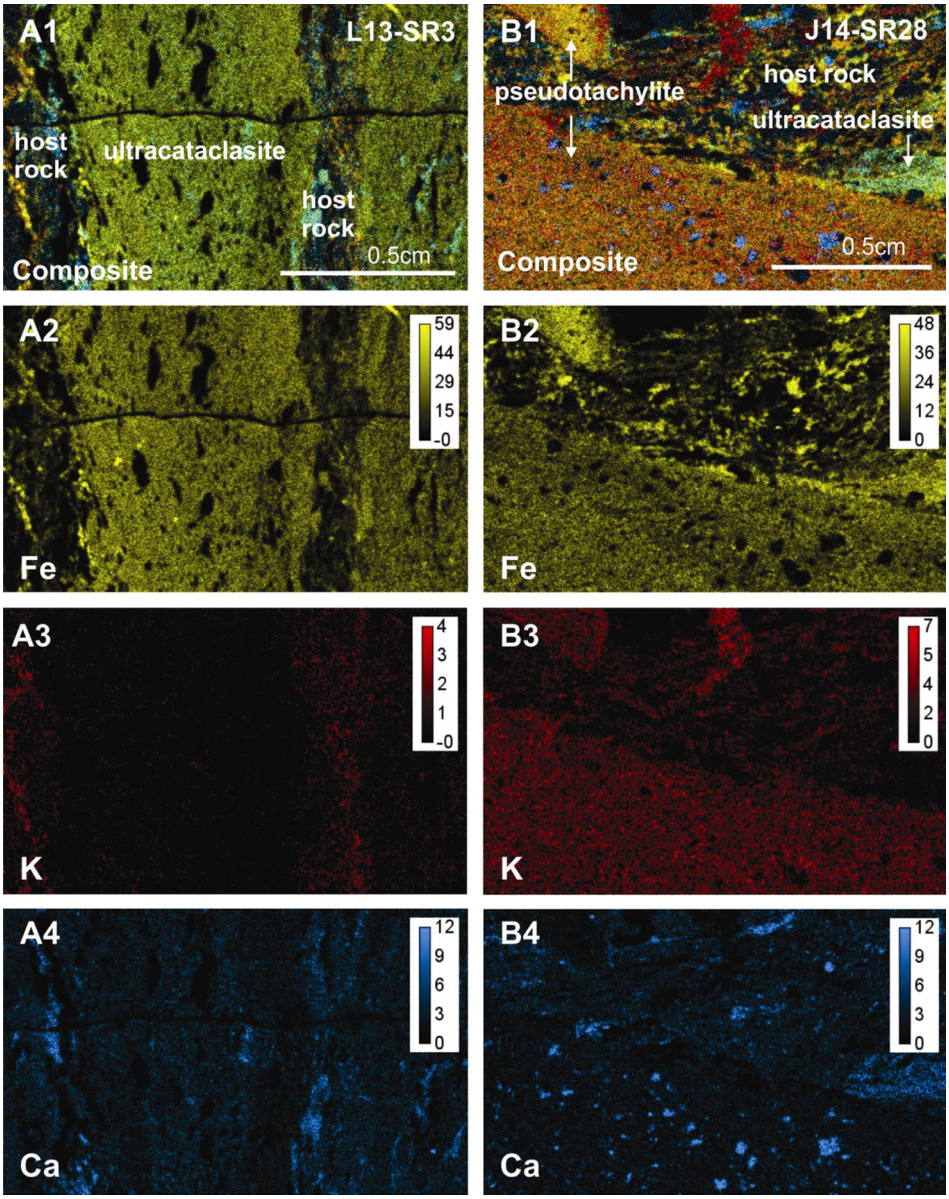

Fig. 6. Micro-XRF map for thick billets of ultracataclasite (A1–4) and pseudotachylite (B1–4) veins in host granitoid. A2–4 and B2–4 are maps for single element (yellow = Fe, red = K and blue = Ca). Color bars represent XRF intensity (cps/mA). A1 and B1 are composite maps created by merging the three elemental maps from the same sample. Blue areas correspond to high abundance of plagioclase; yellow and red areas both correspond to high abundance of mafic minerals, with the red areas highlighting the existence of biotite. As a color merging effect, the orange areas correspond to high abundance of biotite, and the green areas correspond to co-existence of both mafic minerals and plagioclase. (For interpretation of the references to color in this figure legend, the reader is referred to the web version of this article.)

istry of the brittle deformation products. The micro-XRF mapping shows that ultracataclasites and pseudotachylites are both enriched in Fe compared with the host rock. However, the ultracataclasites are relatively enriched in Ca, indicating contribution of plagioclase during cataclasis, while the pseudotachylites are enriched in K (Fig. 6), indicating contribution of biotite to the frictional melt.

Results for major element concentrations from in situ analyses are plotted in Fig. 7A and B. We compared the chemical composition of the pseudotachylites and ultracataclasites with the bulk composition of the host, and the composition of its major mineral phases (plagioclase, quartz, hornblende and biotite). In Fig. 7A and B, each data point of the pseudotachylite, ultracataclasite and hornblende represents one LA-ICP-MS analysis. Pseudotachylite and ultracataclasite data display a large spread due to compositional heterogeneity caused by unavoidable small mineral fragments in the matrix. However, the overall trend shows that the pseudotachylites, ultracataclasites and the host mylonites are compositionally different but genetically linked. In Fig. 7A, we plot (FeO + MgO + TiO_2) (wt%) vs SiO_2 (wt%) to distinguish between mafic (hornblende and biotite) and felsic components (feldspar and quartz): higher mafic component is characterized by low SiO_2 and high FeO + MgO + TiO_2, whereas felsic components are characterized by high SiO_2 and low FeO + MgO + TiO_2. We also plot (Fe + Mg)/(Al + Ti) molar ratios versus K/(Ca + K + Na) molar ratios to distinguish between different mafic minerals, e.g., hornblende and biotite. Biotite has high K but low Ca relative to hornblende, therefore samples enriched in biotites plot on the right (Fig. 7B). The plots show that the ultracataclasites and pseudotachylites are depleted in SiO_2 relative to the host rock, with their compositions falling on a mixing array between biotite and the host rock. The pseudotachylites, however, are much more mafic and their composition approaches that of biotite. What is clear is that the brittle deformation products do not derive from homogeneous deformation of the host

rock; instead, the deformation products appear to preferentially incorporate biotite, especially in the pseudotachylites.

To better quantify the contribution of different minerals to the pseudotachylite melt, we made an inverse mass balance calculation, recasting the major-element composition of the pseudotachylite into the major mineral phases in the host rock. We consider quartz, plagioclase and the mafic component as endmembers. The latter includes both hornblende (10%) and biotite (90%), which because of their similar major element compositions, make it difficult to distinguish between the two mafic minerals in the inversion (mass balance calculations with different biotite/hornblende ratios are in Supplementary Table S5, which yield similar results). Assuming that $\mathbf{y_m}$ is a column vector with m rows, where the value in each row is the concentration of major oxide i in the pseudotachylite ($i = SiO_2$, FeO, CaO etc.), $\mathbf{x_n}$ is a column vector with n rows, where the value in each row is the proportion of endmember j in the pseudotachylite ($j =$ quartz, plagioclase or mafic component), and A_{mn} is an $m \times n$ matrix, where the values in each row are the concentration of major oxide i of the three endmembers. Mass balance requires $\mathbf{y_m} = A_{mn}\mathbf{x_n}$, where $\mathbf{x_n}$ can be calculated by transposing, squaring and then inverting the matrix: $\mathbf{x_n} = (A^{\mathrm{T}}A)^{-1}A^{\mathrm{T}}\mathbf{y_m}$ (Albarède, 1995).

Our mass balance inversion results are plotted in Fig. 7C. For reference, we inverted the host tonalitic composition, yielding quartz, plagioclase and mafic components of 30%, 50% and 20% respectively, consistent with field and petrographic observations. In contrast, the ultracataclasites have a ~28% contribution of mafic components and the pseudotachylites have much higher, ~50% mafic components. Plagioclase is enriched in the ultracataclasites but depleted in the pseudotachylites. Quartz is strongly depleted in both brittle deformation products.

Given that we might have a small amount of contamination in the LA-ICP-MS analyses by plagioclase and quartz clasts smaller than the laser spot size, the calculated proportions of mafic component in the ultracataclasites and pseudotachylites are minimum bounds. Because most mafic minerals in the mylonite host, predominantly biotite, are concentrated in the biotite-defined ductile foliation planes, the composition of the ultracataclasites and pseudotachylites indicates preferential involvement of the ductile fabrics during brittle deformation.

7. Discussion

In Sections 5 and 6, we showed that ductile deformation took place in the lower Asbestos Mountain granitoid at near-solidus conditions during the cooling stage of the pluton, resulting in development in biotite-rich proto-mylonite and mylonite fabrics, which then became involved in subsequent brittle deformation. In this section, we discuss how these biotite-rich fabrics behave during brittle deformation, especially the frictional melting process. Based on our geochemical results and previous studies, we explore the nature of frictional melting in a local shear zone (millimeter- to centimeter-scale), as well as potential linkage between the pseudotachylite chemical composition and earthquake dynamics.

7.1. Role of biotite-rich foliation planes in brittle deformation

Mass balance calculations in Section 6 showed that although biotite is enriched in both brittle deformation products, it dominates in the pseudotachylites and is only slightly enriched in the ultracataclasites. Interestingly, the ultracataclasites show moderate enrichment in plagioclase. This compositional heterogeneity implies that ultracataclasite and pseudotachylite are derived from different parts of the host rock, with the ultracataclasites mobilizing and comminuting plagioclase, and the pseudotachylites developing by preferential melting of the biotite-rich planes.

Two alternative (but not mutually exclusive) interpretations on the relation between the ultracataclasites and pseudotachylites can be made from their chemical composition. The first interpretation follows Magloughlin (1992) and Spray (1995), wherein comminution and frictional melting are complementary processes. Specifically, ultracataclasites could be the precursors of pseudotachylites in that pseudotachylites develop from ultracataclasite in a fully-transitional manner during a continuous fault slip. Because phyllosilicate-rich fabrics are weak zones along which deformation is accommodated (Collettini et al., 2009), the slight enrichment of biotite and moderate enrichment of plagioclase in the ultracataclasites indicate that in the original mylonites, brittle deformation initiated on the biotite-rich foliations, which mainly served as preferred slip surfaces. Slip on these foliations may be accommodated by cataclasis in the adjacent plagioclase. As slip continues, the biotite-rich planes themselves become much more strongly involved in fault slip, eventually melting and forming pseudotachylites. Alternatively, fault slip along biotite-rich foliations may start with frictional melting. Ultracataclasites could form at the termination of fault slip, possibly where biotite abundance decreases or the frictional melts escape, either of which would cause the fault to strengthen.

In both interpretations, regardless of whether ultracataclasite is the precursor of pseudotachylite or *vice versa*, biotite-rich foliation planes appear to play an important role in slip initiation and strain localization in both cataclasis and frictional melting processes. In particular, strong enrichment of biotite in the pseudotachylites indicates that plagioclase and quartz did not melt extensively, suggesting thermodynamic constraints from biotite in frictional melting.

7.2. Disequilibrium melting and preferential melting of biotite during frictional heating

Due to the discrepancy in chemical composition between the host rock and pseudotachylite, it has been proposed from experiments and theory that frictional melting is a process of selective melting of hydrous minerals as opposed to whole-rock equilibrium (e.g., eutectoid) melting (Maddock, 1992; Magloughlin and Spray, 1992; Lin and Shimamoto, 1998; Spray, 2010). Our observations confirm these suggestions as eutectic melts of a tonalite or granite would be much more silicic, containing components of quartz, plagioclase and biotite (Fig. 7D). Our observations indicate that the biotite component is significantly over-represented in the pseudotachylite melt compared to expected eutectoid melt compositions.

The thermodynamic implications of equilibrium versus disequilibrium melting are important. Equilibrium melting requires long enough time for all chemical reactions between different mineral phases to run to completion. This results in eutectic melting, in which the rock is melted at a much lower temperature than the melting point of any single mineral phase due to the freezing point depression effect of multicomponent systems, especially those containing some amount of water. In granitoids containing hydrous minerals, the minimum equilibrium melting temperature is ~650 °C (Huang and Wyllie, 1975). More specifically, the characteristic time required for intra-grain chemical equilibrium scales with the square of the characteristic grain size divided by diffusivity. Diffusivity of most major elements in quartz, feldspar and biotite is less than 10^{-16} $m^2\,s^{-1}$ within the temperature range of 600–1200 °C (Cherniak, 2010a, 2010c; Cherniak and Dimanov, 2010). For grain sizes of 10^{-6}–10^{-3} m, the characteristic time for equilibrium is days to millions of years. In contrast, earthquake slip events associated with generation of pseudotachylites are thought to occur on time scales as short as a few seconds or less. On these short timescales, inter-grain equilibrium is impossible to achieve.

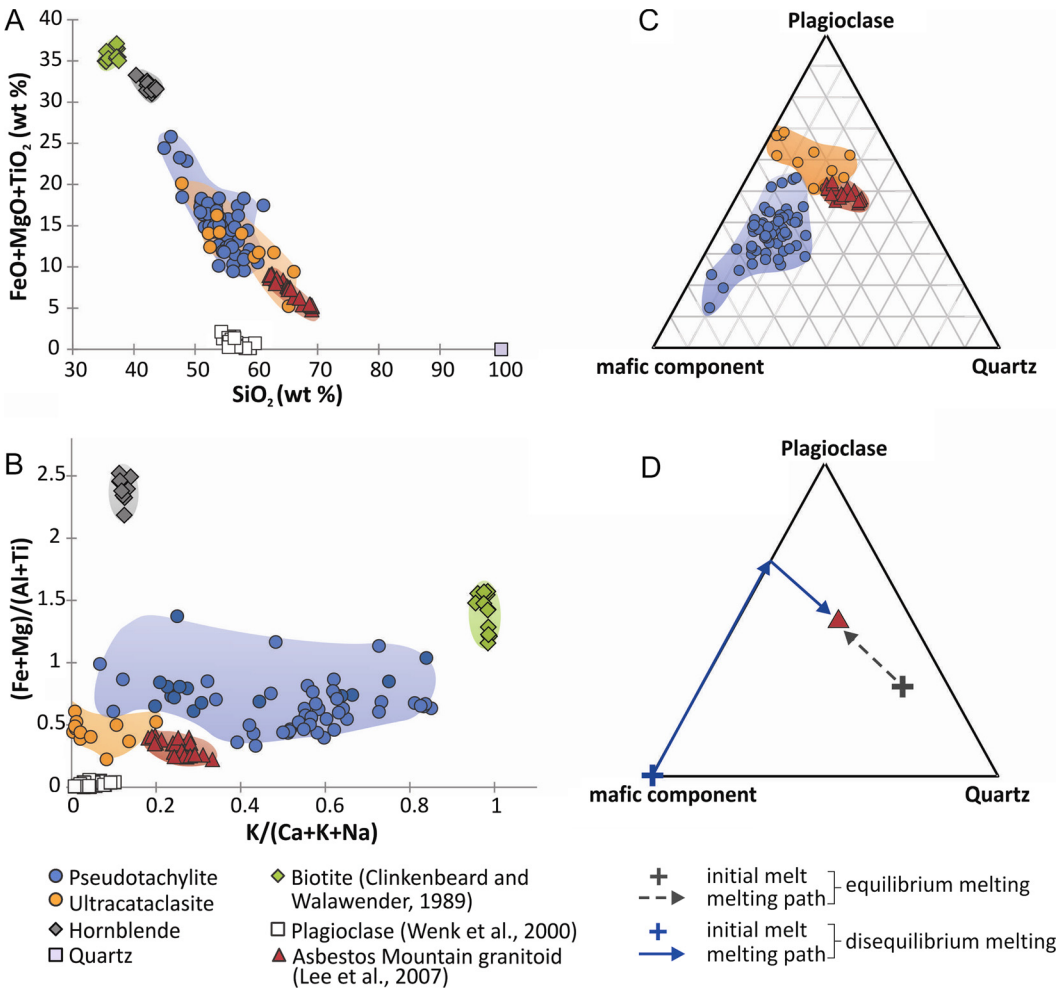

Fig. 7. Composition of the ultracataclasites, pseudotachylites, compared with that of the host granitoids (Lee et al., 2007) and major minerals of quartz, plagioclase (Wenk et al., 2000), biotite (Clinkenbeard and Walawender, 1989) and hornblende (this study). (A) (FeO + MgO + TiO_2) vs SiO_2 (by wt%) plot. Note that the ultracataclasites and pseudotachylites plot along the mixing trend between the host granitoids and mafic minerals. (B) (Fe + Mg)/(Al + Ti) vs K/(Ca + K + Na) (by mole fraction) plot. This plot distinguishes between biotite and hornblende. The pseudotachylites appear to be weighted toward biotite. (C) Mineral composition of the host granitoids, ultracataclasites and pseudotachylites, calculated from geochemical data in (A) and (B) using the inverse mass balance model from Section 6. (D) Schematic diagram showing the initial melt composition and melting path for equilibrium (eutectoid) melting and disequilibrium melting of the host granitoids. In equilibrium melting, the initial melt composition is produced at the eutectic melting point, which is more silicic than the host rock. In disequilibrium melting, the mafic phases are melted first, resulting in a mafic initial melt. Progressive melting of the silicic phases (plagioclase and quartz) will drive the melt composition evolving towards the host rock composition (detailed discussion see Sections 7.2 and 7.3).

As a consequence, disequilibrium melting dominates, wherein the minerals are essentially unaware of each other's presence so that melting follows the melting point of each single phase, bypassing the eutectic melting point (Fig. 7D). Biotite melts at ~800 °C at upper crustal pressures, which is lower than the melting points of plagioclase (~1400 °C) and quartz (~1700 °C) (Robie and Hemingway, 1995; Fleet et al., 2003; Lange et al., 2009) but higher than minimum equilibrium melting temperatures of granitoids. Therefore, biotite is the first phase to melt. Our observation of limited involvement of plagioclase and quartz during frictional melting suggests that the pseudotachylites formed no higher than 1700 °C; the main stage of melting appears to be constrained within a temperature range between 800 °C and 1400 °C.

7.3. Thermodynamics of earthquakes

To explore these concepts in a more physical context, we develop a simple model for temperature evolution in a millimeter- to centimeter-sized shear zone due to shear heating associated with pseudotachylite formation. Fialko and Khazan (2005) developed a model for temperature evolution in a sheared layer, where shearing results in viscous dissipation, and the work done by shear stress τ is converted to frictional heat. The rate of temperature change is controlled by the balance between shear heating (first term on the right in Eq. (1) below), conductive heat loss from the shear zone to the surrounding rock (second term on the right), and consumption of latent heat of fusion for different mineral phases (third term on the right):

$$\frac{\partial T}{\partial t} = \frac{\tau}{C_p \rho}\frac{\partial \epsilon}{\partial t} + \kappa \frac{\partial^2 T}{\partial x^2} - \frac{L}{C_p}\frac{\partial \Phi_m}{\partial t} \tag{1}$$

where $\partial\epsilon/\partial t$ is the strain rate, $\tau\partial\epsilon/\partial t$ is the rate of heat generation, T is the temperature (K), t is the time (s), x (m) is the across-flow coordinate with the origin in the middle of the shear zone ($|x| < w$, w is the half width of the sheared layer, and in our case, the half width of the pseudotachylite vein), κ is the thermal diffusivity ($m^2\,s^{-1}$), C_p is the heat capacity at constant pressure ($J\,kg^{-1}\,K^{-1}$), ρ is the density of the rock or melt in the shear zone ($kg\,m^{-3}$), L is the latent heat of fusion for major minerals in the rock ($J\,kg^{-1}$), Φ_m is the volumetric melt fraction (see Table 1 for definition and values of parameters used in this model).

Table 1
Parameters used in frictional melting model.

Term	Definition and value
A	empirical parameter in viscosity equation (5); $A_{basalt} = 10^{-6}$ Pa s, $A_{rhyolite} = 3.5 \times 10^{-7}$ Pa s (Shaw, 1972)
B	empirical parameter in viscosity equation (5); $B_{basalt} = 2.6 \times 10^4$ K, $B_{rhyolite} = 4.1 \times 10^4$ K (Shaw, 1972)
C	empirical parameter in viscosity equations (6), (7); $C = 2.5$ (Costa, 2005)
C_p	heat capacity (J kg^{-1} K^{-1}); C_p for biotite, plagioclase and quartz are similar, we use $C_p = 1000$ J kg^{-1} K^{-1}
L	latent heat of fusion; $L_{biotite} = 1.6 \times 10^6$ J kg^{-1} (Tumarkina et al., 2011), $L_{plagioclase} = 3 \times 10^5$ J kg^{-1} (Lange et al., 2009), $L_{quartz} = 2 \times 10^5$ J kg^{-1} (Richet et al., 1982)
T	temperature (K); melting temperature for biotite, plagioclase and quartz is 1073 K, 1673 K and 1973 K, respectively (Robie and Hemingway, 1995; Fleet et al., 2003; Lange et al., 2009)
T	time (s)
v	seismic slip rate; $v = 0.1$, 1, 10 m s^{-1}
w	half width of the shear zone/pseudotachylite vein; $w = 0.01$ m
α	empirical parameter in viscosity equations (6), (7); $\alpha = 0.97$
η_0	dynamic viscosity of particle-free melt which is only temperature dependent (Pa s); see equation (5)
η	effective viscosity which is both temperature and melt fraction dependent (Pa s); see equations (6), (7)
ρ	density melt density is $\rho_{melt} = 2.8 \times 10^3$ kg m^{-3}; for individual mineral phases, $\rho_{biotite} = 3 \times 10^3$ kg m^{-3}, $\rho_{quartz} = 2.6 \times 10^3$ kg m^{-3}, $\rho_{plagioclase} = 2.7 \times 10^3$ kg m^{-3}
τ	shear stress (Pa); see equation (4)
Φ_m	volumetric melt fraction
Φ_c	critical volumetric melt fraction below which the material behaves like a solid and over which η/η_0 drops rapidly; see equations (6), (7) $\Phi_c = 0.4$ (Lejeune and Richet, 1995; Costa, 2005)
$\partial\epsilon/\partial t$	strain rate (s^{-1})

Assuming for simplicity a Newtonian rheology, the applied stress is linearly related to the strain rate according to the linear constitutive equation:

$$\tau = \eta \frac{\partial \epsilon}{\partial t} \tag{2}$$

where η is the viscosity (Pa s) of melt in the shear zone.

During an earthquake, the timescales of faulting are usually on the order of seconds, rarely exceeding 2 min (Geller, 1976; Convers and Newman, 2013). On these short timescales, frictional heating is much faster than conductive heat loss, so we can approximate frictional melting as an adiabatic process, wherein no heat is lost from the shear zone (Spray, 1992; Fialko and Khazan, 2005; Spray, 2010). Assuming a constant slip velocity v, the strain rate is then given by $\partial\epsilon/\partial t = \partial v/\partial x = v/w$. This yields the following relationship after combining Eqs. (1) and (2):

$$\frac{\partial T}{\partial t} = \frac{\eta}{C_p \rho}\left(\frac{v}{w}\right)^2 - \frac{L}{C_p}\frac{\partial \Phi_m}{\partial t} \tag{3}$$

Eq. (3) shows that under adiabatic heating, temperature variation depends on slip rate, width of the shear zone, rock rheology (viscosity) and evolving melt fraction.

We solve Eq. (3) from the onset of melting, that is, the initial condition is $T = T_m$ for $t = 0$, where T_m is the melting point of biotite. Because individual phases are melted, the temperature during melting of a particular phase remains constant ($\partial T/\partial t = 0$) due to consumption of latent heat. Only after a phase is consumed by melting will temperature rise, in which case the temperature rises to the melting point of the phase with the next lowest melting point. Therefore we can partition the melting process into stages at which either melt is being generated at constant temperature, or the shear zone is being heated up with no additional melt production.

When melting an individual mineral phase, latent heat is consumed. During this stage, we assume that melt production rate $\partial\Phi_m/\partial t$ is approximately constant. Given that $\partial T/\partial t = 0$, the time for complete melting of a mineral phase i (e.g. biotite, plagioclase and quartz) can be solved from Eq. (3):

$$\Delta t_i = \frac{L\rho}{\eta}\left(\frac{w}{v}\right)^2 \Phi_i \tag{4}$$

where Φ_i is the volumetric proportion of mineral phase i in the melted rock.

As temperature rises and melt is generated, the rheology of the shear zone changes accordingly. The viscosity of the particle-free melt decreases with increasing temperature, which can be described by an Arrhenius-type equation:

$$\eta_0 = A \exp\left(\frac{B}{T}\right) \tag{5}$$

where A and B are empirical constants dependent on melt composition. Because the composition of the pseudotachylites is initially close to that of basalt, we applied a basaltic viscosity to the melt (Shaw, 1972). Values of A and B are listed in Table 1.

During frictional melting, the shear zone transforms from a particle supported system to a melt supported system as melt is generated. The rheology of the shear zone thus shifts from solid-like to liquid-like. A critical melt fraction term Φ_c is used to describe this solid–liquid transition. Φ_c is related to maximum particle packing and is ~0.4 (Lejeune and Richet, 1995). When melt fraction is below the critical melt fraction ($\Phi_m < \Phi_c$), particle interactions dominate, resulting in solid-like behavior and high effective viscosity; when melt fraction is above the critical melt fraction ($\Phi_m > \Phi_c$), particle interactions decrease significantly, resulting in liquid-like behavior and rapid drop in viscosity at higher Φ_m.

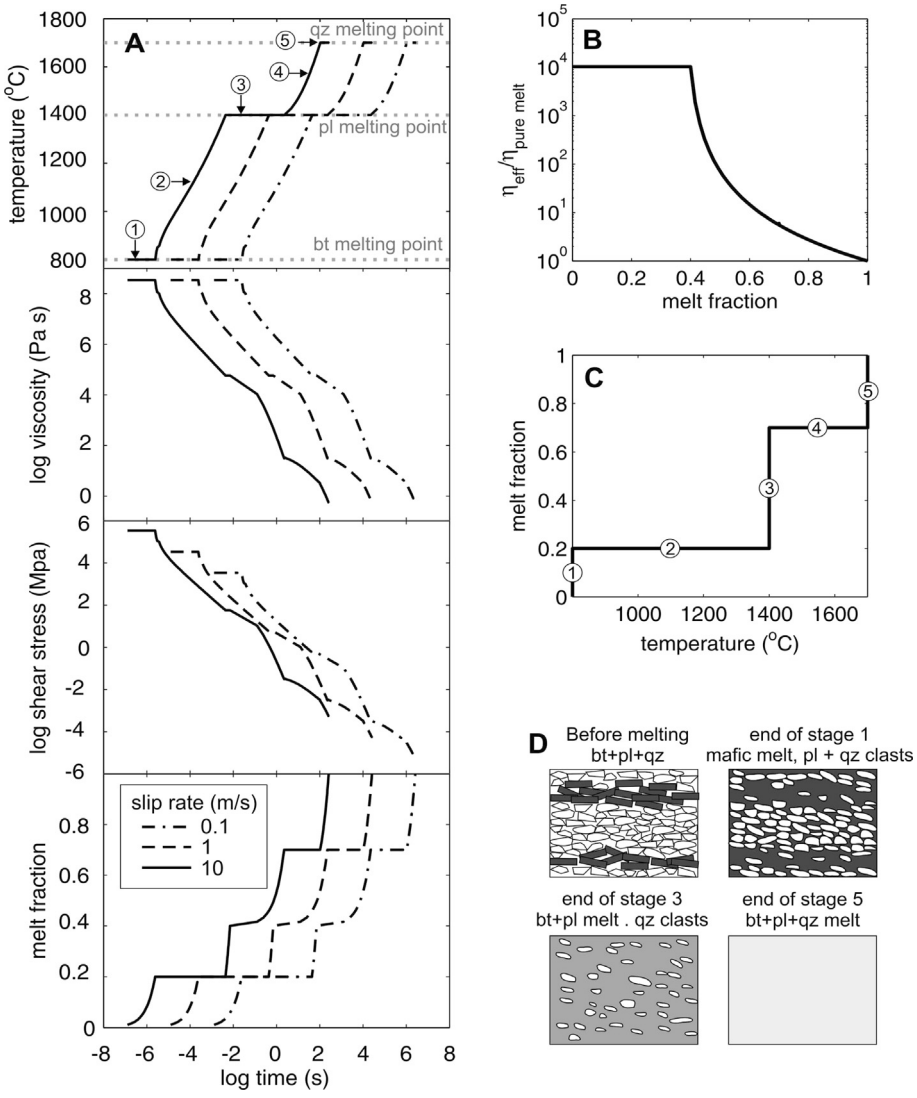

Fig. 8. (A) Evolution of temperature, viscosity, stress and melt fraction in a shear zone ($w = 1$ cm) during frictional melting. A basaltic melt was assumed for modeling viscosity. Labels 1–5 correspond to stages 1–5 in the discussion section. (B) Relation between the effective viscosity and melt fraction. (C) Melt fraction evolution with temperature in the model. (D) Schematic diagram of compositional evolution during frictional melting.

When $\Phi_m > \Phi_c$, the strong dependency of effective viscosity on melt fraction is given by Costa (2005):

$$\eta = \eta_0 \left(1 - \alpha \frac{1-\Phi_m}{1-\Phi_c}\right)^{-C/\alpha} \tag{6}$$

The relation between η/η_0 and Φ_m is plotted in Fig. 8.

When $\Phi_m < \Phi_c$, the effective viscosity is insensitive to the melt fraction and is taken as a constant. Under these conditions, the effective viscosity η is related to the viscosity of particle-free melt η_0, given by the following equation adopted from Costa (2005)

$$\eta = \eta_0 (1-\alpha)^{-C/\alpha} \tag{7}$$

where C is variously referred to as the Einstein's coefficient and takes the value of 2.5, α is an empirical constants which depend on strain rate, particle shapes and particle size distribution. At high strain rate ($>10^{-4}$ s^{-1}), in highly concentrated suspension of rigid monosized particles, η/η_0 is around 10^4 (Caricchi et al., 2007), corresponding to $\alpha \approx 0.97$. We note, however, that there are few experimental results for effective viscosity of partially melted rock at low melt fraction and high strain rate, so the actual value for η/η_0 at $\Phi_m < \Phi_c$ is not well constrained. This uncertainty in η/η_0 will result in errors in the absolute stress and timescales of heating (Eqs. (2)–(4)), but will not change the basic physics.

In high velocity rotary shear experiments, frictional melt is produced at seismic slip rates of $v = 0.1$–10 m s^{-1} (Spray, 1995; Lin and Shimamoto, 1998; Di Toro et al., 2006). In Fig. 8, we modeled evolution of temperature, viscosity, shear stress and melt fraction for a typical pseudotachylite vein developed ($w = 10^{-2}$ m) under different slip rates ($v = 0.1$, 1, and 10 m s^{-1}). We used the mineral composition of the mylonite as the initial composition (20% biotite, 50% plagioclase and 30% quartz). For completeness, we ran our model until the rock was 100% molten. The melting process can be divided into five stages:

Stage 1. Biotite melting is initiated, resulting in generation of mafic melt. Temperature remains constant at the melting point of biotite until all the biotite is consumed. Because the melt fraction is initially lower than Φ_c, viscosity is calculated using Eq. (6), which is a constant value at $\sim 10^7$ Pa s.

Stage 2. After all the biotite is consumed, the shear zone, which now contains mafic melt and clasts of plagioclase and quartz, heats up to the melting point of plagioclase. During this rise in temperature, the melt fraction does not change. However, due to rapid

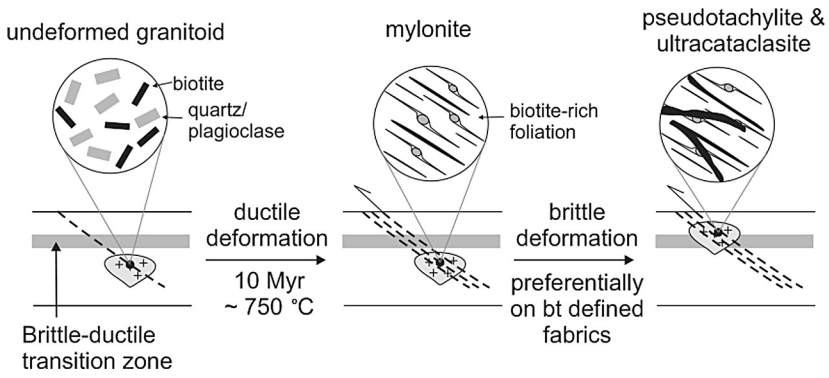

Fig. 9. Schematic diagram for the evolution of the shear zone in the lower Asbestos Mountain granitoid. The magma was initially emplaced at the ductile deformation zone and deformed at near solidus conditions (~750 °C) over a 10 Ma interval, resulting in development of biotite-rich mylonitic fabrics. Later the pluton was uplifted to the brittle deformation zone, where brittle deformation initialized at the weak fabrics, resulting in dark pseudotachylite and ultracataclasite veins superimposing on the mylonites.

temperature rise, viscosity drops significantly, resulting in large stress drop.

Stage 3. The temperature reaches the melting point of plagioclase and stays at 1400 °C until all the plagioclase is consumed. As more melt is introduced into the shear zone, the melt fraction exceeds Φ_c and the effective viscosity decreases (Eq. (7)), resulting in a further drop in shear stress.

Stages 4 and 5 are similar to Stages 2 and 3. The shear zone containing melt of biotite and plagioclase and clasts of quartz heats up until finally all the quartz is melted. Additional stress drop occurs, but is much smaller in both rate and magnitude compared with those in previous stages, mainly because the reduced viscosity imparted by increased melt fraction and higher temperatures decreases the energy dissipation rate (e.g. power) associated with frictional heating.

Our model predicts a large stress drop occurs after all biotite is melted (Stage 2), e.g. ~10 GPa at $v = 1$ m/s. This suggests that the biotite-rich layers become weaker and will have significant strain localization on them during frictional melting. The magnitude of stress drop depends on the effective viscosity and strain rate (v/w). As discussed above, uncertainties in the parameterization η/η_0 with melt fraction may result in large errors on calculated stress drops. However, regardless of these errors, the temperature effect on viscosity alone results in at least 10^3 Pa s decrease in melt viscosity as the biotite-rich melt heats up to the melting point of plagioclase, leading to up to a few MPa stress drop. Therefore uncertainties in our parameterizations of η/η_0 will not change our conclusion that strain localizes on biotite-rich layers.

After biotite is melted, if slip continues further, the shear zone can evolve from Stage 1 to 5, resulting in the melt composition becoming more felsic as plagioclase and quartz begin melting and contributing to the originally basaltic melt. Progressive melting will result in the melt composition evolving from basaltic to andesitic, eventually approaching the composition of the host rock (Fig. 8D). However, on earthquake timescales (less than 2 min) (Geller, 1976; Convers and Newman, 2013), only biotite can be completely melted. Some fraction of plagioclase can be melted if the slip rate is high ($v > 1$ m/s). The time to reach the melting point of quartz is on the order of minutes or more, hence melting of quartz is rarely achieved. In fact, as predicted in our model, the melt viscosity gets lower at elevated temperature and higher melt fraction, which relieves the driving shear stress, thereby the seismic slip can be shut down much sooner than the temperature will reach quartz melting point. As in our case study, only limited amounts of plagioclase may even melt. This explains why frictional melts in felsic host rock generally have basaltic compositions. In summary, our model predicts that the composition of frictional melts evolve with slip time: the longer the slip, the more the melt composition converges toward the bulk rock composition of the host. It has been suggested that, seismic slip duration and slip rates correlate with earthquake magnitude (Geller, 1976; Bizzarri, 2012). It follows that because pseudotachylite composition may be related to slip duration, one potential application of our frictional melt evolution model is that pseudotachylite chemical compositions could be used to constrain the magnitude of paleo-earthquakes. That is, in earthquakes with low slip velocity and short duration, any pseudotachylite generated should be mafic. Pseudotachylites produced in earthquakes with high slip rate and longer duration should have compositions more similar to the host rock.

8. Conclusions

Petrological and geochemical analyses of ductile and brittle deformation products from sheared rocks in the Asbestos Mountain granitoid in California (USA) show that ductile deformation and brittle deformation are closely linked. The ductile deformation lasted more than 10 My at near solidus temperatures of ~750 °C, during which proto-mylonitic and mylonitic fabrics were formed in the last stages of a crystallizing pluton through recrystallization and re-orientation of biotite crystals. Brittle deformation took place later, when the pluton cooled well below solidus temperatures, resulting in development of mafic ultracataclasites and pseudotachylites in the mylonites (Fig. 9). The mafic composition of these brittle deformation products, especially the pseudotachylites, requires a significant contribution from biotite. This suggests that brittle deformation may preferentially initiate on biotite-rich foliation planes in the host mylonite, perhaps because biotite foliation planes are weak.

Frictional heating along the fault plane could eventually lead to melting. Our results show that frictional melting is a disequilibrium process in which the lowest melting point phases (~800 °C), such as biotite, melt first, but such temperatures are still higher than the minimum melting points of hydrous granitoids under equilibrium conditions (~650 °C). Such melting leads to a substantial drop in viscosity, resulting in a large stress drop.

With progressive slip, the melt composition evolves towards the host rock composition as minerals with higher melting points are sequentially melted. The fact that the pseudotachylites in the mylonitized Asbetos Mountain granitoid are strongly enriched in mafic component but depleted in quartz indicates that local shear zone temperatures rarely reached the point of melting quartz, the mineral with the highest melting point. These compositional constraints indicate that frictional heating occurred between 800 and 1400 °C during the earthquake. Nevertheless, this composition–time relation of the pseudotachylites indicates that small, short-duration earthquakes will result in more mafic pseudotachylites, while large, long duration earthquakes will result in more felsic

pseudotachylites. Therefore pseudotachylite compositions can potentially be used to constrain paleo-earthquake source properties.

Acknowledgements

This work was supported by a NSF grant to study the role of continental arcs in long term climate evolution to Lee (OCE-1338842). This work represents one tiny step in our efforts to understand how magmatism, tectonism and exhumation influence the rise and fall of continental arcs. We thank D.M. Morton and T.-C. Lee for introducing us to the Eastern Peninsular Ranges mylonite zone. Brad Hacker and an anonymous reviewer provided insightful comments. Monica Erdman, Claudia Sayao-Valladares, Michael Farner, and Xun Yu are thanked for helping us in the field.

Appendix A. Supplementary material

Supplementary material related to this article can be found online at http://dx.doi.org/10.1016/j.epsl.2015.08.027.

References

Ague, J.J., Brimhall, G.H., 1988. Magmatic arc asymmetry and distribution of anomalous plutonic belts in the batholiths of California: effects of assimilation, crustal thickness, and depth of crystallization. Geol. Soc. Am. Bull. 100, 912–927.

Albarède, F., 1995. Introduction to Geochemical Modeling. Cambridge University Press.

Aleinikoff, J.N., Wintsch, R.P., Tollo, R.P., Unruh, D.M., Fanning, C.M., Schmitz, M.D., 2007. Ages and origins of rocks of the Killingworth Dome, south-central Connecticut: implications for the tectonic evolution of southern New England. Am. J. Sci. 307, 63–118.

Bizzarri, A., 2012. Rupture speed and slip velocity: what can we learn from simulated earthquakes. Earth Planet. Sci. Lett. 317–318, 196–203.

Caricchi, L., Burlini, L., Ulmer, P., Gerya, T., Vassalli, M., Papale, P., 2007. Non-Newtonian rheology of crystal-bearing magmas and implications for magma ascent dynamics. Earth Planet. Sci. Lett. 264, 402–419.

Cherniak, D.J., 2010a. Cation diffusion in feldspars. Rev. Mineral. Geochem. 72, 691–733.

Cherniak, D.J., 2010b. Diffusion in accessory minerals: zircon, titanite, apatite, monazite and xenotime. Rev. Mineral. Geochem. 72, 827–869.

Cherniak, D.J., 2010c. Diffusion in quartz, melilite, silicate perovskite, and mullite. Rev. Mineral. Geochem. 72, 735–756.

Cherniak, D.J., Dimanov, A., 2010. Diffusion in pyroxene, mica and amphibole. Rev. Mineral. Geochem. 72, 641–690.

Clinkenbeard, J.P., Walawender, M.J., 1989. Mineralogy of the La Posta pluton: implications for the origin of zoned plutons in the eastern Peninsular Ranges batholith, southern and Baja California. Am. Mineral. 76, 1258–1269.

Collettini, C., Niemeijer, A., Viti, C., Marone, C., 2009. Fault zone fabric and fault weakness. Nature 462, 907–910.

Convers, J.A., Newman, A.V., 2013. Rapid earthquake rupture duration estimates from teleseismic energy rates, with application to real-time warning. Geophys. Res. Lett. 40, 5844–5848.

Costa, A., 2005. Viscosity of high crystal content melts: dependence on solid fraction. Geophys. Res. Lett. 32, 1–5.

Di Toro, G., Hirose, T., Nielsen, S., Pennacchioni, G., Shimamoto, T., 2006. Natural and experimental evidence of melt lubrication of faults during earthquakes. Science 311, 647–649.

Di Toro, G., Pennacchioni, G., Nielsen, S., 2009. Pseudotachylytes and earthquake source mechanics. In: Fukuyama, E. (Ed.), Fault-Zone Properties and Earthquake Rupture Dynamics. In: Int. Geophys. Ser., vol. 94, pp. 87–133.

Erskine, B.G., Wenk, H.-R., 1985. Evidence for Late Cretaceous crustal thinning in the Santa Rosa mylonite zone, southern California. Geology 13, 274–277.

Farner, M.J., Lee, C.-T.A., Putirka, K.D., 2014. Mafic–felsic magma mixing limited by reactive processes: a case study of biotite-rich rinds on mafic enclaves. Earth Planet. Sci. Lett. 393, 49–59.

Fialko, Y., Khazan, Y., 2005. Fusion by earthquake fault friction: stick or slip. J. Geophys. Res. 110.

Fleet, M.E., Deer, W.A., Howie, R.A., Zussman, J., 2003. Rock-Forming Minerals, vol. 3A: Micas. Geological Society of London.

Gao, S., Liu, X., Yuan, H., Hattendorf, B., Günther, D., Chen, L., Hu, S., 2002. Determination of forty two major and trace elements in USGS and NIST SRM glasses by laser ablation–inductively coupled plasma–mass spectrometry. Geostand. Newsl. 26, 181–196.

Geller, R.J., 1976. Scaling relations for earthquake source parameters and magnitudes. Bull. Seismol. Soc. Am. 66, 1501–1523.

Goodwin, L.B., Renne, P.R., 1991. Effects of progressive mylonitization on Ar retention in biotites from the Santa Rosa mylonite zone, California, and thermochronologic implications. Contrib. Mineral. Petrol. 108, 283–297.

Hammarstrom, J.M., Zen, E.-A., 1986. Aluminum in hornblende: an empirical igneous geobarometer. Am. Mineral. 71, 1297–1313.

Hayden, L.A., Watson, E.B., Wark, D.A., 2008. A thermobarometer for sphene (titanite). Contrib. Mineral. Petrol. 155, 529–540.

Huang, W.-L., Wyllie, P.J., 1975. Melting reactions in the system $NaAlSi_3O_8$–$KAlSi_3O_8$–SiO_2 to 35 kilobars, dry and with excess water. J. Geol. 83, 737–748.

Jaffey, A.H., Flynn, K.F., Glendenin, L.E., Bentley, W.C., Essling, A.M., 1971. Precision measurement of half-lives and specific activities of ^{235}U and ^{238}U. Phys. Rev. C 4, 1889–1906.

Lange, R.A., Frey, H.M., Hector, J., 2009. A thermodynamic model for the plagioclase-liquid hygrometer/thermometer. Am. Mineral. 94, 494–506.

Lee, C.-T.A., Bachmann, O., 2014. How important is the role of crystal fractionation in making intermediate magmas? Insights from Zr and P systematics. Earth Planet. Sci. Lett. 393, 266–274.

Lee, C.-T.A., Morton, D.M., Farner, M.J., Moitra, P., 2015. Field and model constraints on silicic melt segregation by compaction/hindered settling: the role of water and its effect on latent heat release. Am. Mineral. 100, 1762–1777.

Lee, C.-T.A., Morton, D.M., Kistler, R.W., Baird, A.K., 2007. Petrology and tectonics of Phanerozoic continent formation: from island arcs to accretion and continental arc magmatism. Earth Planet. Sci. Lett. 263, 370–387.

Lee, J.K.W., Williams, I.S., Ellis, D.J., 1997. Pb, U and Th diffusion in natural zircon. Nature 390, 159–162.

Lejeune, A.-M., Richet, P., 1995. Rheology of crystal-bearing silicate melts: an experimental study at high viscosities. J. Geophys. Res. 100, 4215–4229.

Lin, A., Shimamoto, T., 1998. Selective melting processes as inferred from experimentally generated pseudotachylytes. J. Asian Earth Sci. 16, 533–545.

Ludwig, K.R., 2012. Isoplot 3.75. A Geochronological Toolkit for Microsoft Excel. Berkeley Geochronol. Center Spec. Publ., vol. 5.

Maddock, R.H., 1983. Melt origin of fault-generated pseudotachylytes demonstrated by textures. Geology 11, 105–108.

Maddock, R.H., 1992. Effects of lithology, cataclasis and melting on the composition of fault-generated pseudotachylytes in Lewisian gneiss, Scotland. Tectonophysics 204, 261–278.

Magloughlin, J.F., 1992. Microstructural and chemical changes associated with cataclasis and frictional melting at shallow crustal levels: the cataclasite–pseudotachylyte connection. Tectonophysics 204, 243–260.

Magloughlin, J.F., Spray, J.G., 1992. Frictional melting processes and products in geological materials: introduction and discussion. Tectonophysics 204, 197–206.

Morton, D.M., Miller, F.K., Kistler, R.W., Premo, W.R., Lee, C.-T.A., Langenheim, V.E., Wooden, J.L., Snee, L.W., Clausen, B.L., Cossette, P., 2014. Framework and petrogenesis of the northern Peninsular Ranges batholith, southern California. Mem. Geol. Soc. Amer. 211, 61–143.

Niemeijer, A., Marone, C., Elsworth, D., 2010. Fabric induced weakness of tectonic faults. Geophys. Res. Lett. 37.

Pittarello, L., Pennacchioni, G., Di Toro, G., 2012. Amphibolite-facies pseudotachylytes in Premosello metagabbro and felsic mylonites (Ivrea Zone, Italy). Tectonophysics 580, 43–57.

Premo, W.R., Morton, D.M., Wooden, J.L., Fanning, C.M., 2014. U–Pb zircon geochronology of plutonism in the northern Peninsular Ranges batholith, southern California: implications for the Late Cretaceous tectonic evolution of southern California. In: Morton, D.M., Miller, F.K. (Eds.), Peninsular Ranges Batholith, Baja California and Southern California. In: Mem. Geol. Soc. Amer., vol. 211, pp. 145–180.

Richet, P., Bottinga, Y., Denielou, L., Petitet, J.P., Tequi, C., 1982. Thermodynamic properties of quartz, cristobalite and amorphous SiO_2: drop calorimetry measurements between 1000 and 1800 K and a review from 0 to 2000 K. Geochim. Cosmochim. Acta 46, 2639–2658.

Robie, R.A., Hemingway, B.S., 1995. Thermodynamic properties of minerals and related substances at 298.15 K and 1 bar (10^5 pascals) pressure and at higher temperature. U.S. Geol. Surv. Bull. 2131.

Rowe, C.D., Kirkpatrick, J.D., Brodsky, E.E., 2012. Fault rock injections record paleoearthquakes. Earth Planet. Sci. Lett. 335–336, 154–166.

Schmidt, M.W., 1992. Amphibole composition in tonalite as a function of pressure: an experimental calibration of the Al-in-hornblende barometer. Contrib. Mineral. Petrol. 110, 304–310.

Schmitz, M.D., Bowring, S.A., 2001. U–Pb zircon and titanite systematics of the Fish Canyon Tuff: an assessment of high-precision U–Pb geochronology and its application to young volcanic rocks. Geochim. Cosmochim. Acta 65, 2571–2587.

Shaw, H.R., 1972. Viscosities of magmatic silicate liquids: an empirical method of prediction. Am. J. Sci. 272, 870–893.

Sibson, R.H., 1975. Generation of pseudotachylyte by ancient seismic faulting. Geophys. J. R. Astron. Soc. 43, 775–794.

Simpson, C., 1984. Borego Springs–Santa Rosa mylonite zone: a Late Cretaceous west-directed thrust in southern California. Geology 12, 8–11.

Spencer, K.J., Hacker, B.R., Kylander-Clark, A.R.C., Andersen, T.B., Cottle, J.M., Stearns, M.A., Poletti, J.E., Seward, G.G.E., 2013. Campaign-style titanite U–Pb dating by laser-ablation ICP: implications for crustal flow, phase transformations and titanite closure. Chem. Geol. 341, 84–101.

Spray, J.G., 1992. A physical basis for the frictional melting of some rock-forming minerals. Tectonophysics 204, 205–221.

Spray, J.G., 1995. Pseudotachylyte controversy: fact or friction? Geology 23, 1119–1122.

Spray, J.G., 2010. Frictional melting processes in planetary materials: from hypervelocity impact to earthquakes. Annu. Rev. Earth Planet. Sci. 38, 221–254.

Stacey, J.S., Kramers, J.D., 1975. Approximation of terrestrial lead isotope evolution by a two-stage model. Earth Planet. Sci. Lett. 26, 207–221.

Todd, V.R., Erskine, B.G., Morton, D.M., 1988. Metamorphic and tectonic evolution of the northern Peninsular Ranges Batholith, southern California. In: Ernst, W.G. (Ed.), Metamorphism and Crustal Evolution of the Western United States (Rubey Volume 7), pp. 894–937.

Tumarkina, E., Misra, S., Burlini, L., Connolly, J.A.D., 2011. An experimental study of the role of shear deformation on partial melting of a synthetic metapelite. Tectonophysics 503, 92–99.

Wenk, H.-R., Johnson, L.R., Ratschbacher, L., 2000. Pseudotachylites in the eastern peninsular ranges of California. Tectonophysics 321, 253–277.

Wiedenbeck, M., Alle, P., Corfu, F., Griffin, W.L., Roddick, J.C., Spiegel, W., 1995. Three natural zircon standards for U–Th–Pb, Lu–Hf, trace element and REE analyses. Geostand. Newsl. 19, 1–23.